ROYAL SOCIETY
OF CHEMISTRY

PAPER

Check for updates

A tuned Lewis acidic catalyst guided by hard–soft acid–base theory to promote N₂ electroreduction†

Yongwen Ren, Chang Yu,* Xuedan Song, [ID] Fengyi Zhou, Xinyi Tan, Yiwang Ding, Qianbing Wei, Jiafu Hong and Jieshan Qiu [ID] *

The electrocatalytic N₂ reduction reaction (NRR) to ammonia (NH₃) driven by intermittent renewable electricity under ambient conditions offers an alternative to the energy-intensive Haber–Bosch process. However, as a distinct core of the process, the design strategy of the electrocatalyst for enhancing the N₂ activation ability is still in a trial-and-error stage due to the absence of theoretical guidance. As a result, the corresponding NH₃ yield rate and selectivity are much lower than that required for implementation at scale. In this work, on the basis of the hard–soft acid–base theory, we report a paradigm for the design of an electrocatalyst with tuned Lewis acidity to efficiently activate and reduce N₂ to NH₃. As a proof of concept, it is revealed that enhancing the Lewis acidity of the molybdenum sulfide (MoS$_x$) model catalyst supported on carbon nanotubes can greatly improve its activation ability toward the N₂ molecule. Accordingly, a high faradaic efficiency of 21.60 ± 2.35% and NH₃ yield rate of 40.4 ± 3.6 μg h^{-1} mg$_{cat.}$$^{-1}$ are obtained over the modified MoS$_x$, which are ∼2 times enhanced in comparison with the original MoS$_x$, respectively. Density functional theory calculations verify that the electron transfer from the occupied σ orbitals of N₂ to the empty d orbitals of Mo sites within MoS$_x$ can be greatly accelerated by tuning the Lewis acidity of MoS$_x$ to match with the basicity of N₂, thereby enhancing the N₂ activation process *via* the σ → d donation mechanism.

Introduction

Ammonia (NH₃) is extremely imperative for fertilizer production, and also can be used as an appealing energy carrier, which is mainly produced through the Haber–Bosch process at present.[1,2] However, this technique requires a pure H₂ feedstock and is driven by high temperature (400–600 °C) and pressure (200–350 atm), which consumes ∼2% of the global energy supply and produces large amounts of greenhouse gases.[3,4] By comparison, the electrocatalytic N₂ reduction reaction (NRR) is a highly encouraging route for the sustainable production of NH₃ because it can be ideally operated at mild conditions with intermittent renewable electricity as the driving force and water as the hydrogen source.[5–7]

The electrochemical synthesis of NH₃ has been explored for a long time since the late 1960s, and has recently developed rapidly.[8] Unfortunately, this technology is still far from the large-scale implementation at present. The main obstacle toward progress is the extreme inertness of the N₂ molecule with the high dissociation enthalpy (941 kJ mol^{-1}), low proton

affinity (493.8 kJ mol^{-1}), and large gap (10.8 eV) between the highest occupied molecular orbital (HOMO) and lowest unoccupied molecular orbital (LUMO).[9–11] Besides, the selectivity of the NRR process is also plagued by the competing H₂ evolution with fast kinetics. Although extensive strategies of design for electrocatalysts have been presented, including vacancy engineering, heteroatom doping, strain engineering, and crystal facet engineering, the present activation ability of a catalyst for the N₂ molecule remains insufficient due to the lack of theoretical guidance, resulting in relatively low faradaic efficiency (FE) and yield rate of NH₃.[12–17] Thus, to resolve this bottleneck, it is highly required to develop the design concept of an electrocatalyst for improving their activation ability towards the N₂ molecule. If the N₂ activation process can be efficiently enhanced, the subsequent proton-coupled electron transfer steps will be greatly accelerated, finally facilitating the whole NRR process and really speeding up this cutting-edge field.[9,18,19]

Fundamentally speaking, the N₂ molecule owning two lone-pair electrons is a typical Lewis hard base, and therefore usually acts as the electron donor in chemical reactions.[9,20] According to the hard–soft acid–base (HSAB) theory that the hard and soft base preferentially interact with the hard and soft acid, respectively (Fig. S1†), the N≡N bond can be effectively activated by the Lewis hard acid sites of catalysts *via* the electron "donating–accepting" effects.[21] Recently, a map of transition

metal-based catalysts, such as Mo, Fe, Co, and Pd, has been presented for the NRR process.[22–25] It was found that the metal active sites and the carbon support (*e.g.*, carbon nanotubes, graphene, graphdiyne) both synergistically enhanced the NRR performance.[26–30] Although great progress has been made, the present N_2 activation ability is still inadequate, which greatly limits the practical applications of this emerging technique. Notably, the transition metals with d orbitals are apt to lose the electrons and become the Lewis acid sites.[31–33] Therefore, it can be speculated that if the electron structures of transition metal-based catalysts can be rationally adjusted to form the hard acid sites, which match with the basicity of the N_2 molecule, their N_2 activation ability will be greatly enhanced. Accordingly, the whole NRR process will be well boosted.

Herein, as a proof of concept, we take a molybdenum sulfide (MoS_x) with abundant Mo^{5+} sites (Lewis soft sites) as the model catalyst to investigate the critical impact of the Lewis acidity on the N_2 activation process. The Lewis acidity of the Mo sites in an as-made sample is greatly increased *via* partial substitution of sulfur with oxygen atoms (denoted as MoS_x-O) that have a larger electronegativity value of 3.44 compared with that of sulfur (2.58) (Scheme 1). Doing so enables us to obtain a high NRR FE of 21.60 ± 2.35% and NH_3 yield rate of 40.4 ± 3.6 μg h^{-1} mg$_{cat.}$$^{-1}$. As a control/proof, the Lewis acidity of Mo sites is also reversely decreased by partially replacing the sulfur atoms with phosphorus atoms (2.19 for the electronegativity value, denoted as MoS_x-P) that are less electronegative than sulfur, and a deteriorated NRR performance is demonstrated (Scheme 1). The combined experimental results demonstrate that to achieve the enhanced N_2 activation and accelerated NRR process, the Lewis acidity of the catalysts should match with the Lewis basicity of the N_2 molecule. Density functional theory (DFT) calculations further revealed that the Mo sites with Lewis acid features can effectively delocalize the localized electron of the N_2 molecule, and then activate the N_2 molecule *via* the σ → d donation mechanism.
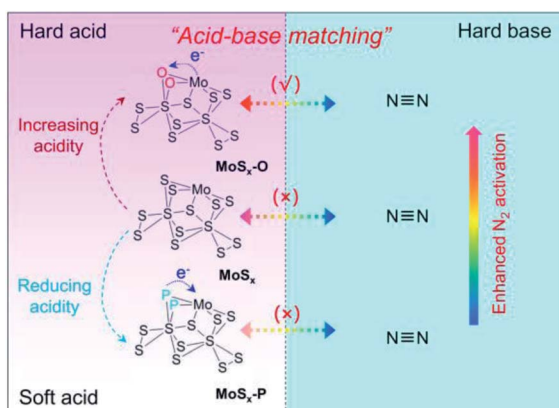
Results and discussion

Synthesis and characterization of the MoS_x catalyst

The MoS_x/CNTs was prepared *via* acid precipitation method at room temperature by using multiwalled carbon nanotubes (CNTs) as the conductive additive. Subsequently, it was annealed at 200 °C for 2 hours in argon (Ar) gas.[34,35] After that, the as-obtained MoS_x/CNTs was further oxidized in air atmosphere at 200 °C for 60 min, resulting in the formation of MoS_x-O$_{60}$/CNTs (Fig. 1a). To elucidate the critical role of the oxygen content in tuning the Lewis acidity of the Mo sites, a suite of control samples, including MoS_x-O$_{10}$/CNTs, MoS_x-O$_{30}$/CNTs, and MoS_x-O$_{90}$/CNTs, were also prepared by changing the oxidation time (10, 30, and 90 min, respectively). Thermogravimetric analysis (TGA) shows that the content of CNTs in MoS_x/CNTs and MoS_x-O$_{60}$/CNTs is ~10 wt% (Fig. S2†). Scanning electron microscopy (SEM) and transmission electron microscopy (TEM) images indicate that the MoS_x species in MoS_x/CNTs and MoS_x-O$_{60}$/CNT$_x$s uniformly coat on the surface of CNTs (Fig. S3†). The high-resolution transmission electron microscopy (HRTEM) and the selected area electron diffraction (SAED) characterizations reveal that the MoS_x species in MoS_x/CNTs and MoS_x-O$_{60}$/CNTs exhibit poor crystallization, which is further evidenced by the X-ray diffraction (XRD) analysis (Fig. S4 and S5†). The SEM energy dispersive X-ray spectroscopy (SEM-EDS) elemental mapping confirms that the MoS_x-O$_{60}$/CNTs
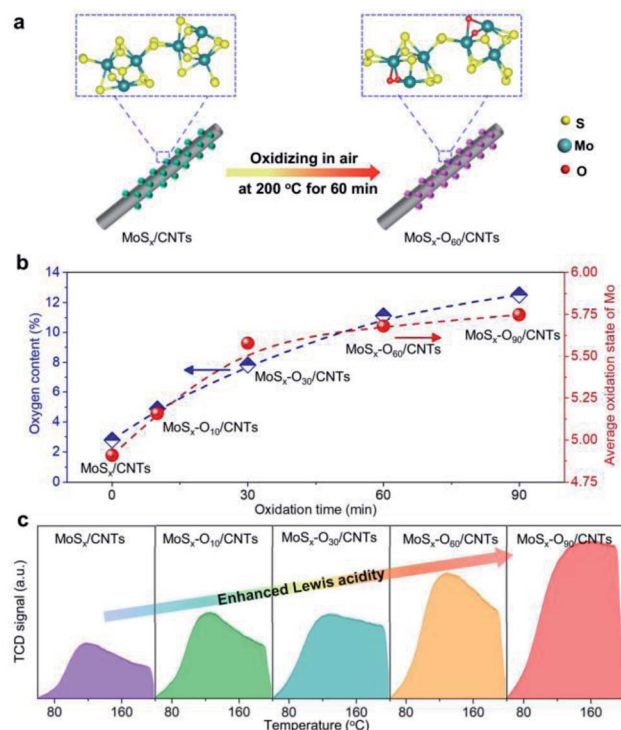

Fig. 1 (a) Schematic synthesis for the MoS_x-O$_{60}$/CNTs catalyst by the thermal oxidation method. (b) The variations of the oxygen content and average oxidation state of Mo *versus* oxidation time for the as-made samples derived from XPS analysis. (c) NH_3-TPD curves for MoS_x/CNTs, MoS_x-O$_{10}$/CNTs, MoS_x-O$_{30}$/CNTs, MoS_x-O$_{60}$/CNTs, and MoS_x-O$_{90}$/CNTs.

Scheme 1 Illustration for the proposed "acid–base matching" paradigm to enhance/decrease the activation ability of the MoS_x electrocatalyst toward the N_2 molecule, including increasing/reducing the Lewis acidity by partially replacing the S atom within MoS_x with O (MoS_x-O)/P atoms (MoS_x-P).

This journal is © The Royal Society of Chemistry 2021

J. Mater. Chem. A, 2021, **9**, 13036–13043 | **13037**

owns a higher content of O element compared with MoS_x/CNTs, preliminarily elucidating the successful introduction of the O element (Fig. S6†). Correspondingly, a new broad peak at 800–990 cm^{-1} originating from the Mo–O bond is detected in the Raman spectrum of MoS_x-O_{60}/CNTs in comparison to that of MoS_x/CNTs, further verifying the incorporation of the O element (Fig. S7†).[34,36,37] X-ray photoelectron spectroscopy (XPS) spectra confirm the existence of C, S, O, and Mo elements in MoS_x/CNTs, MoS_x-O_{10}/CNTs, MoS_x-O_{30}/CNTs, MoS_x-O_{60}/CNTs, and MoS_x-O_{90}/CNTs, which is also consistent with the SEM-EDS results (Fig. S8†). The detailed content of Mo, S, and O elements and corresponding atomic ratios of the samples derived from the XPS analyses are summarized in Table S1.† It can be clearly seen that the atomic ratio of Mo to S for MoS_x/CNTs is 1 : 2.75, which is almost consistent with the literature, whereas such a value gradually reduces with the prolongation of the oxidation time.[34] Correspondingly, the O content progressively improves from 2.87 to 11.12% with the extension of the oxidation time from 0 to 60 min, and then slightly increases when further increasing the oxidation time to 90 min (12.51%) (Fig. 1b). Furthermore, a new peak with the electron binding energy (BE) of 530.0 eV that can be attributed to the lattice oxygen is detected in the high-resolution O 1s spectra for the oxidized samples, and the ratio of its integral area to that of adsorbed oxygen increases with the increment of the oxidation time (Fig. S9†).[38] Meanwhile, the high-resolution XPS spectra of Mo 3d for the samples are also given in Fig. S9.† It can be clearly seen that the Mo 3d spectrum of MoS_x/CNTs exhibits two doublet peaks, including a weak doublet with the electron binding energy (BE) of 228.7/231.7 eV ascribed to Mo^{4+} 3d components and a strong doublet with the electron BE of 229.4/232.5 eV belonging to Mo^{5+} 3d components.[39–41] As for the oxidized samples, a new doublet assigned to Mo^{6+} 3d components is observed at the electron BE of 231.8/235.3 eV due to the incorporation of the O elements.[42] Furthermore, a decreased content of Mo^{5+}, along with an increased content of Mo^{6+}, is distinctly demonstrated with the prolongation of the oxidation time. Moreover, the high-resolution Mo 3d XPS depth-profile study of MoS_x-O_{60}/CNTs confirms that an oxidation layer with a certain thickness is formed over the surface of MoS_x-O_{60}/CNTs after the oxidation treatment (Fig. S10†). The detailed changes for the average oxidation state of Mo are depicted in Fig. 1b. A similar variation tendency for the average oxidation state of Mo and the content of O is verified. In particular, the Mo average oxidation state evidently improves from 4.91 to 5.75 with the prolongation of the oxidation time from 0 to 90 min. The results indicate that the Lewis acidity of the Mo sites in the MoS_x species can be regulated by this thermal oxidation method. To further confirm this point, the temperature-programmed desorption of ammonia (NH_3-TPD) was conducted. It can be seen from Fig. 1c that the integral area of the NH_3 desorption peak associated with the Lewis acidity significantly increases as the oxidation time increases, which is in accordance with the XPS analyses. On the basis of the HASB theory and the results above, it can be imagined that there possibly exists a sample that can match well with the basicity of the N_2 molecule, thereby enhancing the activation ability for N_2 and facilitating the whole NRR process.

Electrochemical NRR measurements

All electrochemical NRR tests were investigated in a modified H-type cell using 0.1 M KOH aqueous solution as the electrolyte under ambient conditions, wherein a salt bridge was employed to avoid the possible diffusion of ammonia and maintained the charge balance of the electrolyte (Fig. S11†).[43] Before the test, the purified N_2 gas was bubbled in a cathodic chamber for 30 min, and then the electrochemical NRR test was conducted under the continuous feeding of N_2. After electrolysis for 2 h, the electrolyte was collected and then the produced ammonia was detected by Nessler reagent and indophenol blue methods (Fig. S12†). The Watt and Chrisp method was employed to determine the by-product hydrazine (N_2H_4) (Fig. S13†). It should be pointed out that all of the applied potentials mentioned in this work were converted into the values *versus* reversible hydrogen electrode (*vs.* RHE).

The linear sweep voltammetry (LSV) curves over MoS_x-O_{60}/CNTs reveal that the presented current density in the N_2-saturated electrolyte is larger than that in the Ar-saturated electrolyte among the applied potential range of 0.05 to −0.25 V, primarily confirming the NRR activity of MoS_x-O_{60}/CNTs. Then, the difference of the NRR performance between MoS_x/CNTs and MoS_x-O_{60}/CNTs was elaborately investigated, and the corresponding current density profiles and ultraviolet-visible (UV-Vis) absorption spectra are displayed in Fig. S14 and S15,† respectively. As shown in Fig. 2b, the faradaic efficiency (FE) of NRR over MoS_x/CNTs gradually improves from 5 ± 1.93% to 12.73 ± 1.93% with the rise of the applied potential from −0.05 to −0.15 V. Further increasing the applied potential to −0.25 V, the corresponding FE rapidly declines, mainly attributed to the competition of the hydrogen evolution reaction (HER). By contrast, the MoS_x-O_{60}/CNTs electrocatalyst with higher Lewis acidity delivers a ~2-fold enhancement of FE (21.60 ± 2.35%) at the same potential of −0.15 V. A peak value of 40.4 ± 3.6 μg h^{-1} $mg_{cat.}^{-1}$ for the NH_3 yield rate is achieved by MoS_x-O_{60}/CNTs at −0.15 V, which is ~1.5 folds higher than that achieved by MoS_x/CNTs (25.9 ± 3.6 μg h^{-1} $mg_{cat.}^{-1}$) (Fig. 2c). The NRR performance of the as-obtained MoS_x-O_{60}/CNTs is also superior in comparison with most of the previously reported Mo-based electrocatalysts (Table S2†). To confirm the source of ammonia, a sequence of rigorous control experiments was carried out with the MoS_x-O_{60}/CNTs as an example. It was found that the ammonia is only detected in the electrolyte by using MoS_x-O_{60}/CNTs as the electrocatalyst under N_2 atmosphere, further confirming that the produced ammonia is not from the air, the feeding N_2, the electrolyte, and the MoS_x-O_{60}/CNTs itself, but from the NRR process (Fig. S16†). Meanwhile, the by-product N_2H_4 is not detected in the electrolytes acquired at the applied potentials above (Fig. S17†).

Additionally, the concentration of produced ammonia was quantitatively determined with ^1H nuclear magnetic resonance (^1H NMR) by employing the isotope labeling of $^{15}N_2$ as the
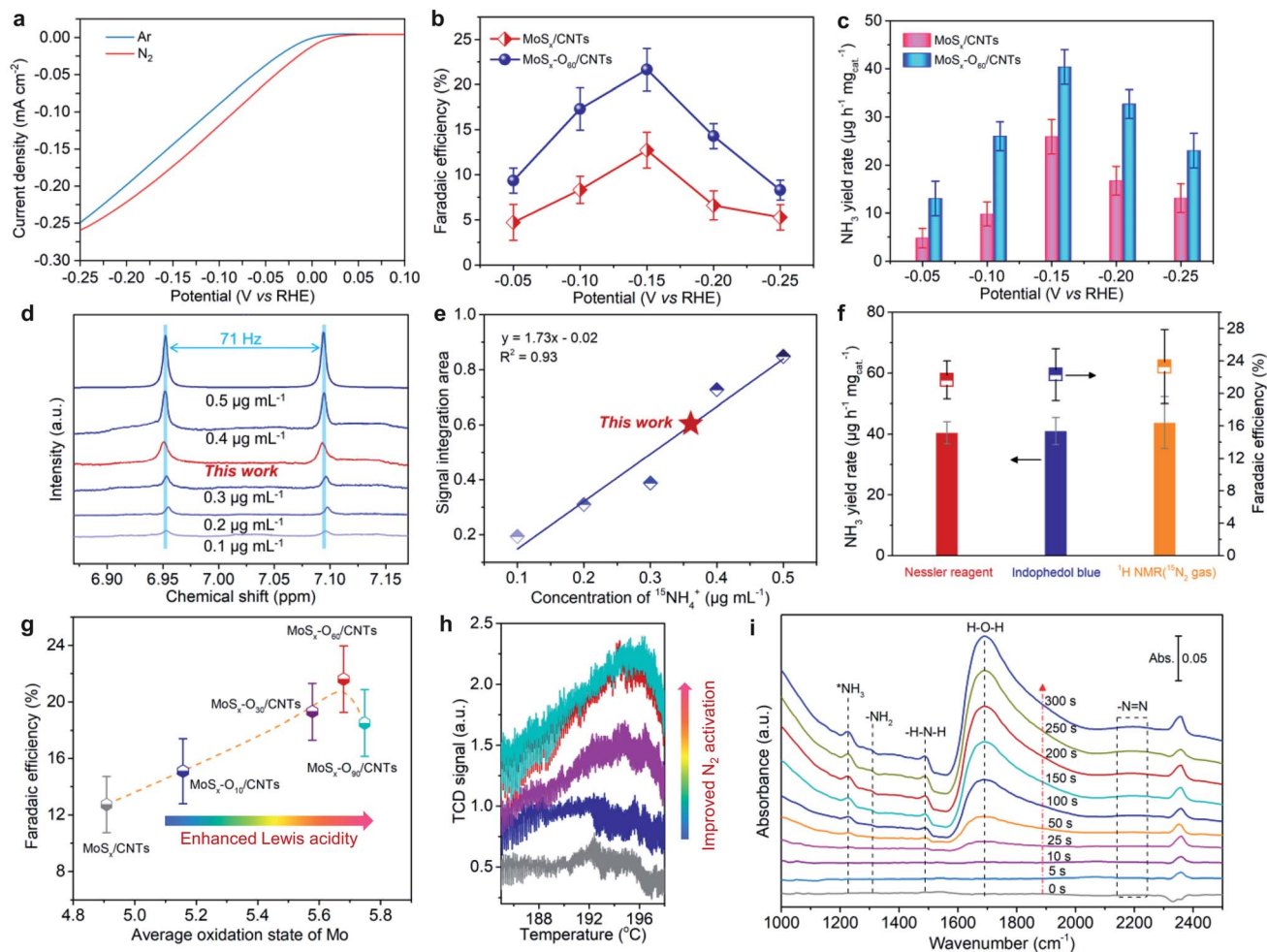
13038 | *J. Mater. Chem. A*, 2021, **9**, 13036–13043

This journal is © The Royal Society of Chemistry 2021

Fig. 2 (a) LSV curves of MoS_x-O_{60}/CNTs measured in Ar- and N_2-saturated electrolytes. (b and c) The obtained FEs and NH_3 yield rates for MoS_x/CNTs and MoS_x-O_{60}/CNTs at different potentials of −0.05, −0.10, −0.15, −0.20, and −0.25 V vs. RHE, respectively. (d) ^1H NMR spectra of the standard solutions with various $^{15}NH_4^+$ concentrations and the electrolyte obtained using MoS_x-O_{60}/CNTs as the electrocatalyst at −0.15 V under $^{15}N_2$ atmosphere for 2 h (denoted as this work). (e) The corresponding calibration curve for isotopically labelled $^{15}N_2$ experiment in view of the $^{15}NH_4^+$ concentrations and the integration areas. (f) Comparison of FEs and NH_3 yield rates determined by Nessler reagent, indophenol blue, and ^1H NMR (using $^{15}N_2$ as the feeding gas) methods, respectively. (g) The correlation between FEs and average oxidation states of Mo for the as-made samples. (h) N_2-TPD profiles of MoS_x/CNTs (gray curve), MoS_x-O_{10}/CNTs (navy curve), MoS_x-O_{30}/CNTs (purple curve), MoS_x-O_{60}/CNTs (red curve), and MoS_x-O_{90}/CNTs (aqua curve). (i) Time-resolved in $situ$ electrochemical ATR-FTIR spectra over MoS_x-O_{60}/CNTs at −0.15 V vs. RHE in 0.1 M KOH under N_2 atmosphere.

feeding gas (Fig. 2d and e).[44] As depicted in Fig. 2f, the FEs and NH_3 yield rates obtained from the Nessler reagent, indophenol blue, and ^1H NMR methods agree well with each other, adequately verifying the accuracy of the quantification for the produced ammonia. In addition, the catalytic stability of MoS_x-O_{60}/CNTs was evaluated by consecutive cycling tests (Fig. S18a†). It was found that the corresponding NRR FE and NH_3 yield rate exhibit a slight reduction after five cycles, particularly reaching 18.4% (85.2% of retention) and 35.1 μg h^{-1} $mg_{cat.}^{-1}$ (86.9% of retention) in the fifth cycle, respectively (Fig. S18b†). Furthermore, no obvious changes in the structure and composition of MoS_x-O_{60}/CNTs can be observed after five consecutive cycles by TEM, XRD, and Raman spectroscopy characterizations, indicative of the good stability of MoS_x-O_{60}/CNTs in the NRR process (Fig. S19†).

The results above indicate that the enhancement of Lewis acidity for the as-made sample has a positive impact on the NRR performance to some degree. To better illustrate this point, we associated the average oxidation state of Mo in all samples with their NRR FEs, and a volcano plot was obtained (Fig. 2g). The FE exhibits an upward tendency with the increase of the average oxidation state of Mo from 4.91 to 5.68, and then decreases with the further increment of the Mo average oxidation state to 5.75. A peak value of 21.60 ± 2.35% for FE is presented over MoS_x-O_{60}/CNTs with the Mo average oxidation state of 5.68, indicative of the optimal Lewis acidity towards N_2 activation. To probe the specific impact of Lewis acidity on the N_2 activation ability for the samples, the temperature-programmed desorption of N_2 (N_2-TPD) was then performed (Fig. S20†). As shown in Fig. 2h, a desorption peak of N_2 is detected in the range of 186 to 198 °C,

This journal is © The Royal Society of Chemistry 2021

J. Mater. Chem. A, 2021, **9**, 13036–13043 | **13039**

and ascribed to the chemisorption of N_2 molecules over the as-made electrocatalysts. Moreover, the present activation ability of the as-made samples for N_2 is significantly enhanced with the increase of the Mo average oxidation state from 4.91 to 5.68, corresponding to the improvement of the Lewis acidity. The activation ability for N_2 remains almost unchanged upon further increasing the Lewis acidity (MoS_x-O_{90}/CNTs). The above results indicate that the MoS_x-O_{60}/CNTs owns the optimal Lewis hard acid sites that can match well with the basicity of the dN_2 molecule (Lewis hard base). As a result, the N≡N triple bond can be effectively activated by the Lewis hard acid sites *via* the electron "donating–accepting" effects, eventually resulting in a greatly boosted NRR performance.[45–47] To further demonstrate the crucial role of Lewis acidity of MoS_x material for N_2 activation process, a significant control sample, phosphorus (P) doped MoS_x (MoS_x-P/CNTs) was also prepared by the low-temperature phosphating method. Since the phosphorus has a smaller electronegativity value of 2.19 compared with that of sulfur (2.58), it is easier to lose electrons than sulfur and form the decreased Lewis acidity of the Mo sites. The structure and composition of MoS_x-P/CNTs were firstly confirmed by XRD, SEM, and SEM-EDS elemental mapping (Fig. S21 and S22†). The XPS characterization was also carried out to reveal the chemical states of the component elements in MoS_x-P/CNTs. In the P 2p spectrum, a predominant peak of PO_4^{3-} and two weak peaks of the P–Mo bond are detected at 134.2, 130.7, and 129.3 eV, respectively, indicative of the successful introduction of P (Fig. S23a†).[48,49] As for the Mo 3d spectrum of MoS_x-P/CNTs, two doublet peaks including a strong doublet of Mo^{4+} 3d components and a weak doublet of Mo^{5+} 3d components are observed (Fig. S23b†), which is quite different from that of MoS_x/CNTs (Fig. S10†). On the basis of this, the average valence state of Mo in MoS_x-P/CNTs is calculated to be 4.32. As expected, the MoS_x-P/CNTs delivers a deteriorated NRR performance ($7.34 \pm 1.15\%$ for FE and 10.8 ± 2.1 μg h^{-1} mg$_{cat.}^{-1}$ for NH_3 yield rate at -0.15 V) compared with that of the original MoS_x/CNTs (Fig. S24†), indicating that the decrease of Lewis acidity for MoS_x/CNTs is not conducive to the N_2 activation and the whole NRR process. This control experiment adequately verifies that for the purpose of enhancing the N_2 activation process, the Lewis acidity of the catalysts should match with the Lewis basicity of the N_2 molecule. To further investigate the detailed activation mechanism of MoS_x-O_{60}/CNTs toward the N_2 molecule, time-resolved *in situ* electrochemical attenuated total reflectance Fourier transform infrared (ATR-FTIR) spectroscopy was then performed. The corresponding results are diplayed in Fig. 2i. Clearly, the absorption peak for the adsorbed target product of NH_3 (*NH_3) can be observed at 1228 cm^{-1}, and the intensity gradually enhances with increase of electroreduction time from 0 to 300 s, which further verifies that the NH_3 is originated from the electroreduction of N_2 molecules.[50–52] Moreover, the absorption peaks for –N_xH_y intermediates, including –H–N–H bending (1492 cm^{-1}) and –NH_2 wagging vibrations (~1300 cm^{-1}), are gradually enhanced with the increment of the electroreduction time.[50,53] The results strongly confirm that the N_2 molecule can be efficiently activated over the surface of MoS_x-O_{60}/CNTs, and the resultant NRR process follows an associative mechanism.[50]

Electronic structure analysis of electrocatalysts by DFT calculations

In addition, the DFT calculations were conducted to verify the electronic structures of the electrocatalysts and gain an insightful understanding for the mechanism of N_2 activation at an atomic scale. Since the atom ratio of Mo to S within MoS_x/CNTs is 1 : 2.75 (Table S1†), corresponding to the MoS_3, the structure of MoS_3 is selected as the structural model for MoS_x (Fig. S25†).[54,55] At first, the deformation charge density was carried out to investigate the variation for the valance state of Mo atom in MoS_x material with/without the doping of O atoms. As depicted in Fig. 3, the positive charge is intensively distributed around the Mo atom sites, and the negative charge is mainly located around the S and O atom sites. Furthermore, it was found that the Mo atom of Mo increases to $+1.791|e|$ after replacing the one S atom by one O atom (donated as 1O-MoS_x). A further improved atomic charge of Mo ($+2.020|e|$) is observed when replacing the two S atoms by two O atoms (donated as 2O-MoS_x). By contrast, the atomic charge of the Mo atom in MoS_x-P/CNTs (taking 2P-MoS_x as the structure model) is only $+1.456|e|$ (Fig. S26†), which is even lower than that in the original MoS_x/CNTs ($+1.638|e|$). The results indicate that the oxygen with a higher electronegativity value of 3.44, in contrast to that of sulfur (2.58) as well as phosphorus (2.19), can attract more electrons from the adjacent Mo atom and effectively delocalize the localized electron of the Mo atom, finally leading to an increased valence state and Lewis acidity of Mo. This is in keeping with the XPS and NH_3-TPD results above.

N_2 activation mechanism over the Lewis acidic sites

Subsequently, we examined the interactions between N_2 molecules and different Mo sites by taking MoS_x and 2O-MoS_x as the examples. It can be clearly found from Fig. 4a and b that the calculated bond length of the N_2 molecule adsorbed in the side-on mode over the Mo sites of MoS_x (1.120 Å) is smaller than that
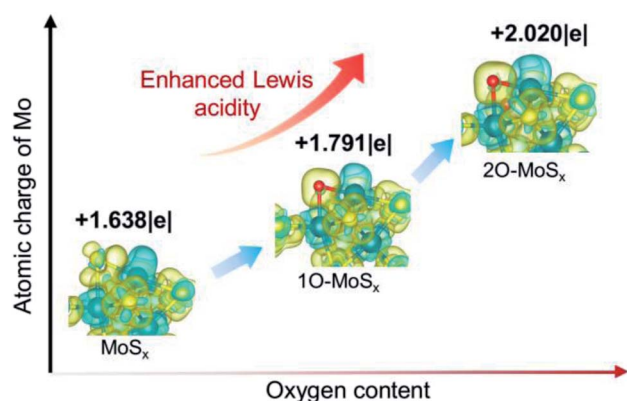

Fig. 3 The isosurfaces of deformation charge density for MoS_x, 1O-MoS_x, and 2O-MoS_x, and the corresponding variation for the atomic charge of Mo derived from Bader charge analysis. Light blue (light yellow) regions represent charge loss (accumulation), and the isosurface is set to be 0.004 e bohr^{-3}. Color scheme: dark green, Mo; yellow, S; red, O.
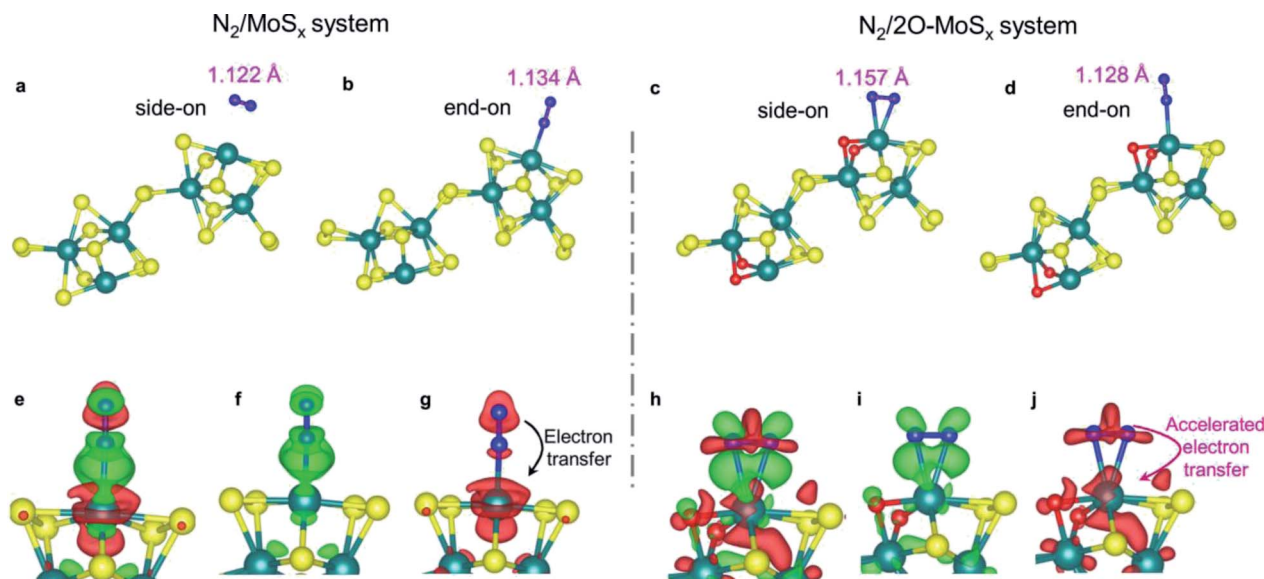
13040 | *J. Mater. Chem. A*, 2021, **9**, 13036–13043

This journal is © The Royal Society of Chemistry 2021

Fig. 4 The configurations and corresponding bond lengths of the adsorbed N_2 molecules in side-on and end-on modes over the Mo atoms of MoS_x (N_2/MoS_x system) (a and b) and $2O-MoS_x$ ($N_2/2O-MoS_x$ system) (c and d), respectively. Charge density difference of N_2/MoS_x (e) and $N_2/2O-MoS_x$ (h) systems, where the charge accumulation and depletion are denoted by green and red, respectively. Color scheme: dark green, Mo; yellow, S; red, O; blue, N. The isosurface is set to be 0.002 e bohr^{-3}. The corresponding charge accumulation and depletion over N_2/MoS_x (f and g) and $N_2/2O-MoS_x$ (i and j) systems are also separately presented.

in the end-on mode (1.134 Å), which means that the end-on mode is the optimal adsorption configuration for the N_2 molecule in the N_2/MoS_x system. On the contrary, the side-on mode is the optimal adsorption configuration for the N_2 molecule in the $N_2/2O-MoS_x$ system, where the bond lengths of the N_2 molecule adsorbed in side-on and end-on modes over the Mo sites of $2O-MoS_x$ are 1.157 and 1.128 Å, respectively (Fig. 4c and d). Additionally, it can be clearly observed that the bond length of the N_2 molecule in the side-on mode (the optimal adsorption) over $2O-MoS_x$ is much larger than that in the end-on mode over MoS_x (the optimal adsorption), which indicates that the Mo sites with higher valence state or Lewis acidity are easier to activate/polarize the N_2 molecule. By contrast, for the $2P-MoS_x$ with distinctly decreased Lewis acidity, the slightly prolonged N≡N bond lengths of 1.128 and 1.130 Å are presented over its surface in the adsorption configurations of end-on and side-on modes, respectively (Fig. S27†). This result further confirms that, to achieve a strong N_2 activation ability, the Lewis acidity of the electrocatalyst should match with the Lewis basicity of the N_2 molecule.

To uncover the detailed activation mechanism toward the N_2 molecule, the charge donation–backdonation process was then visualized *via* the charge density difference analysis (Fig. 4e–j). As given in Fig. 4e, a significant charge accumulation region is observed between the N and Mo atoms of MoS_x, which means that the N_2 molecule can be activated through the Mo–N interaction.[56] The tendency of charge transfer can be qualitatively observed from Fig. 4f and g. Clearly, the charge depletion region is larger than the corresponding charge accumulation region around the N atom far away from Mo atom, verifying that the charge is transferred from the N atom to the adjacent Mo

atom.[56] Accordingly, it can be concluded that the N_2 molecule is easily activated by the Mo sites of MoS_x through the σ → d donation mechanism.[20] As for the $N_2/2O-MoS_x$ system, a larger charge accumulation region is found between Mo and N atoms (Fig. 4h and i) compared with that shown in the N_2/MoS_x system (Fig. 4f), indicative of the stronger activation ability for the N_2 molecule over the Mo sites of $2O-MoS_x$. In addition, as shown in Fig. 4j, the charge depletion region of the N atoms in the $N_2/2O-MoS_x$ system distributes throughout the whole N_2 molecule, and is also slightly larger than that in the N_2/MoS_x system (Fig. 4g), indicating that much more electrons of the N atom are lost and transferred to the adjacent Mo atom. That is to say, the Mo sites with higher valence state or Lewis acidity are much easier to accept the electrons from the N_2 molecule, thereby accelerating the N_2 activation process *via* the σ → d donation mechanism.[57,58] This is also in line with the experimental results.

Conclusions

In summary, a paradigm for the design of an electrocatalyst to improve the N_2 activation and NRR process was presented on the basis of the HSAB theory. The experiments revealed that to achieve a strong N_2 activation ability, the Lewis acidity of the electrocatalyst should match with the Lewis basicity of the N_2 molecule. In particular, the $MoS_x-O_{60}/CNTs$ with enhanced Lewis acidity delivered a NRR FE of $21.60 \pm 2.35\%$ and NH_3 yield rate of 40.4 ± 3.6 μg h^{-1} mg$_{cat.}^{-1}$, ~2 times greater in comparison to that of the original $MoS_x/CNTs$ with low Lewis acidity. The DFT calculations demonstrated that the as-made electrocatalyst with deliberately promoted Lewis acidity accelerated the electron transfer from the occupied σ orbitals of N_2 to

its empty d orbitals and then boosted the activation process of N_2 *via* the σ → d donation mechanism. These findings provide new insight into enhancing the N_2 activation ability of the electrocatalyst toward the N_2 molecule, and may really promote the development of the cutting-edge field.

Conflicts of interest

There are no conflicts to declare.

Acknowledgements

References

1 J. W. Erisman, M. A. Sutton, J. Galloway, Z. Klimont and W. Winiwarter, *Nat. Geosci.*, 2008, **1**, 636–639.

2 C. Smith, A. K. Hill and L. Torrente-Murciano, *Energy Environ. Sci.*, 2020, **13**, 331–344.

3 M. A. Legare, G. Belanger-Chabot, M. Rang, R. D. Dewhurst, I. Krummenacher, R. Bertermann and H. Braunschweig, *Nat. Chem.*, 2020, **12**, 1076–1080.

4 D. R. MacFarlane, P. V. Cherepanov, J. Choi, B. H. R. Suryanto, R. Y. Hodgetts, J. M. Bakker, F. M. Ferrero Vallana and A. N. Simonov, *Joule*, 2020, **4**, 1186–1205.

5 R. F. Service, *Science*, 2014, **345**, 610.

6 G. Marnellos and M. Stoukides, *Science*, 1998, **282**, 98–100.

7 D. Yuan, Z. Wei, P. Han, C. Yang, L. Huang, Z. Gu, Y. Ding, J. Ma and G. Zheng, *J. Mater. Chem. A*, 2019, **7**, 16979–16983.

8 G.-F. Chen, S. Ren, L. Zhang, H. Cheng, Y. Luo, K. Zhu, L.-X. Ding and H. Wang, *Small Methods*, 2018, **3**, 1800337.

9 Y. Huang, D. D. Babu, Z. Peng and Y. Wang, *Adv. Sci.*, 2020, **7**, 1902390.

10 G. Qing, R. Ghazfar, S. T. Jackowski, F. Habibzadeh, M. M. Ashtiani, C. P. Chen, M. R. Smith and T. W. Hamann, *Chem. Rev.*, 2020, **120**, 5437–5516.

11 H. P. Jia and E. A. Quadrelli, *Chem. Soc. Rev.*, 2014, **43**, 547–564.

12 X. Cui, C. Tang and Q. Zhang, *Adv. Energy Mater.*, 2018, **8**, 1800369.

13 S. Wang, F. Ichihara, H. Pang, H. Chen and J. Ye, *Adv. Funct. Mater.*, 2018, **28**, 1803309.

14 B. H. R. Suryanto, H.-L. Du, D. Wang, J. Chen, A. N. Simonov and D. R. MacFarlane, *Nat. Catal.*, 2019, **2**, 290–296.

15 Y. Ren, C. Yu, X. Tan, H. Huang, Q. Wei and J. Qiu, *Energy Environ. Sci.*, 2021, **14**, 1176–1193.

16 S. Luo, X. Li, M. Wang, X. Zhang, W. Gao, S. Su, G. Liu and M. Luo, *J. Mater. Chem. A*, 2020, **8**, 5647–5654.

17 Q. Li, Y. Guo, Y. Tian, W. Liu and K. Chu, *J. Mater. Chem. A*, 2020, **8**, 16195–16202.

18 J. Deng, J. A. Iñiguez and C. Liu, *Joule*, 2018, **2**, 846–856.

19 H. D. Xiaoxi Guo, F. Qu and J. Li, *J. Mater. Chem. A*, 2019, **7**, 3531–3543.

20 M.-A. Légaré, G. Bélanger-Chabot, R. D. Dewhurst, E. Welz, I. Krummenacher, B. Engels and H. Braunschweig, *Science*, 2018, **359**, 896–900.

21 R. G. Pearson, *J. Am. Chem. Soc.*, 1963, **85**, 3533–3539.

22 H. Yu, Y. Xue, L. Hui, C. Zhang, Y. Fang, Y. Liu, X. Chen, D. Zhang, B. Huang and Y. Li, *Natl. Sci. Rev.*, 2020, nwaa213, DOI: 210.1093/nsr/nwaa1213.

23 Y. Fang, Y. Xue, L. Hui, H. Yu and Y. Li, *Angew. Chem., Int. Ed.*, 2021, **60**, 3170–3174.

24 L. Hui, Y. Xue, H. Yu, Y. Liu, Y. Fang, C. Xing, B. Huang and Y. Li, *J. Am. Chem. Soc.*, 2019, **141**, 10677–10683.

25 Y. Fang, Y. Xue, Y. Li, H. Yu, L. Hui, Y. Liu, C. Xing, C. Zhang, D. Zhang, Z. Wang, X. Chen, Y. Gao, B. Huang and Y. Li, *Angew. Chem., Int. Ed.*, 2020, **59**, 13021–13027.

26 A. K. Geim, *Science*, 2009, **324**, 1530–1534.

27 V. Georgakilas, M. Otyepka, A. B. Bourlinos, V. Chandra, N. Kim, K. C. Kemp, P. Hobza, R. Zboril and K. S. Kim, *Chem. Rev.*, 2012, **112**, 6156–6214.

28 Y. Du, W. Zhou, J. Gao, X. Pan and Y. Li, *Acc. Chem. Res.*, 2020, **53**, 459–469.

29 C. Huang, Y. Li, N. Wang, Y. Xue, Z. Zuo, H. Liu and Y. Li, *Chem. Rev.*, 2018, **118**, 7744–7803.

30 Z. Zuo and Y. Li, *Joule*, 2019, **3**, 899–903.

31 L. Huang, J. Wu, P. Han, A. M. Al-Enizi, T. M. Almutairi, L. Zhang and G. Zheng, *Small Methods*, 2018, **3**, 1800386.

32 X. Yu, P. Han, Z. Wei, L. Huang, Z. Gu, S. Peng, J. Ma and G. Zheng, *Joule*, 2018, **2**, 1610–1622.

33 L. Zhang, M. Cong, X. Ding, Y. Jin, F. Xu, Y. Wang, L. Chen and L. Zhang, *Angew. Chem., Int. Ed.*, 2020, **59**, 10888–10893.

34 H. Ye, L. Ma, Y. Zhou, L. Wang, N. Han, F. Zhao, J. Deng, T. Wu, Y. Li and J. Lu, *Proc. Natl. Acad. Sci. U. S. A.*, 2017, **114**, 13091–13096.

35 H. Ye, L. Wang, S. Deng, X. Zeng, K. Nie, P. N. Duchesne, B. Wang, S. Liu, J. Zhou, F. Zhao, N. Han, P. Zhang, J. Zhong, X. Sun, Y. Li, Y. Li and J. Lu, *Adv. Energy Mater.*, 2017, **7**, 1601602.

36 X. Cao, B. Zheng, W. Shi, J. Yang, Z. Fan, Z. Luo, X. Rui, B. Chen, Q. Yan and H. Zhang, *Adv. Mater.*, 2015, **27**, 4695–4701.

37 L. He, W. Zhang, Q. Mo, W. Huang, L. Yang and Q. Gao, *Angew. Chem., Int. Ed.*, 2019, **59**, 3544–3548.

38 S. Gao, S. Sun, Z. Liu, X. Jiao, X. Zu, Q. Hu, Y. Sun, T. Yao, W. Zhang, S. Wei and Y. Xie, *Nat. Commun.*, 2017, **8**, 14503.

39 M. L. Tang, D. C. Grauer, B. Lassalle-Kaiser, V. K. Yachandra, L. Amirav, J. R. Long, J. Yano and A. P. Alivisatos, *Angew. Chem., Int. Ed.*, 2011, **123**, 10385–10389.

40 K. C. Pham, Y. H. Chang, D. S. McPhail, C. Mattevi, A. T. Wee and D. H. Chua, *ACS Appl. Mater. Interfaces*, 2016, **8**, 5961–5971.

41 L. Guo, J. Yu, J. Xiao, A. Li, Z. Yang, L. Zeng, Q. Zhang and Y. Zhu, *Angew. Chem., Int. Ed.*, 2020, **59**, 13071–13078.

42 Y. Deng, L. R. L. Ting, P. H. L. Neo, Y.-J. Zhang, A. A. Peterson and B. S. Yeo, *ACS Catal.*, 2016, **6**, 7790–7798.

43 Y. Ren, C. Yu, X. Tan, X. Han, H. Huang, H. Huang and J. Qiu, *Small Methods*, 2019, **3**, 1900474.

44 S. Z. Andersen, V. Čolić, S. Yang, J. A. Schwalbe, A. C. Nielander, J. M. McEnaney, K. Enemark-Rasmussen, J. G. Baker, A. R. Singh, B. A. Rohr, M. J. Statt, S. J. Blair, S. Mezzavilla, J. Kibsgaard, P. C. K. Vesborg, M. Cargnello, S. F. Bent, T. F. Jaramillo, I. E. L. Stephens, J. K. Nørskov and I. Chorkendorff, *Nature*, 2019, **570**, 504–508.

45 Y. Li, Y. Fang, Y. Xue, Y. Li, H. Yu, L. Hui, Y. Liu, C. Xing, C. Zhang, D. Zhang, Z. Wang, X. Chen, Y. Gao and B. Huang, *Angew. Chem., Int. Ed.*, 2020, **59**, 13021–13027.

46 T. Ling, Y. Yang, L. Zhang, Z. Hu, Y. Zheng, C. Tang, P. Chen, R. Wang, K. Qiu, J. Mao and S. Z. Qiao, *Angew. Chem., Int. Ed.*, 2020, **59**, 4525–4531.

47 Y. Tong, H. Guo, D. Liu, X. Yan, J. Liang, P. Su, S. Zhou, J. Liu, G. Q. M. Lu and S. X. Dou, *Angew. Chem., Int. Ed.*, 2020, **59**, 7356–7361.

48 J. Kibsgaard and T. F. Jaramillo, *Angew. Chem., Int. Ed.*, 2014, **53**, 14433–14437.

49 C.-J. Chen, V. Veeramani, Y.-H. Wu, A. Jena, L.-C. Yin, H. Chang, S.-F. Hu and R.-S. Liu, *Appl. Catal., B*, 2020, **263**, 118259.

50 C.-C. Zhang, X. Liu, Y.-P. Liu and Y. Liu, *Chem. Mater.*, 2020, **32**, 8724–8732.

51 Y. Yao, S. Zhu, H. Wang, H. Li and M. Shao, *Angew. Chem., Int. Ed.*, 2020, **59**, 10479–10483.

52 H.-B. Wang, J.-Q. Wang, R. Zhang, C.-Q. Cheng, K.-W. Qiu, Y.-j. Yang, J. Mao, H. Liu, M. Du, C.-K. Dong and X.-W. Du, *ACS Catal.*, 2020, **10**, 4914–4921.

53 C. Lv, L. Zhong, Y. Yao, D. Liu, Y. Kong, X. Jin, Z. Fang, W. Xu, C. Yan, K. N. Dinh, M. Shao, L. Song, G. Chen, S. Li, Q. Yan and G. Yu, *Chem*, 2020, **6**, 2690–2702.

54 P. D. Tran, T. V. Tran, M. Orio, S. Torelli, Q. D. Truong, K. Nayuki, Y. Sasaki, S. Y. Chiam, R. Yi, I. Honma, J. Barber and V. Artero, *Nat. Mater.*, 2016, **15**, 640–646.

55 D. Escalera-López, Z. Lou and N. V. Rees, *Adv. Energy Mater.*, 2019, **9**, 1802614.

56 R. Kumar and A. K. Singh, *ChemCatChem*, 2020, **12**, 5456–5464.

57 F. Lai, N. Chen, X. Ye, G. He, W. Zong, K. B. Holt, B. Pan, I. P. Parkin, T. Liu and R. Chen, *Adv. Funct. Mater.*, 2020, **30**, 1907376.

58 Q. Qin, Y. Zhao, M. Schmallegger, T. Heil, J. Schmidt, R. Walczak, G. Gescheidt-Demner, H. Jiao and M. Oschatz, *Angew. Chem., Int. Ed.*, 2019, **58**, 13101–13106.

This journal is © The Royal Society of Chemistry 2021

J. Mater. Chem. A, 2021, **9**, 13036–13043 | **13043**